

The JCMT BISTRO-2 Survey: The Magnetic Field in the Center of the Rosette Molecular Cloud

VERA KÖNYVES,¹ DEREK WARD-THOMPSON,¹ KATE PATTLE,² JAMES DI FRANCESCO,^{3,4} DORIS ARZOUMANIAN,⁵
ZHIWEI CHEN,⁶ PHAM NGOC DIEP,⁷ CHAKALI ESWARAIH,^{8,9} LAPO FANCIULLO,¹⁰ RAY S. FURUYA,^{11,12} THIEM HOANG,^{13,14}
CHARLES L. H. HULL,^{15,16,17} JIHYE HWANG,^{13,14} DOUG JOHNSTONE,^{3,4} JI-HYUN KANG,¹³ JANIK KAROLY,¹
FLORIAN KIRCHSCHLAGER,¹⁸ JASON M. KIRK,¹ PATRICK M. KOCH,¹⁰ JUNGMI KWON,¹⁹ CHANG WON LEE,^{13,14}
TAKASHI ONAKA,^{20,19} JEAN-FRANÇOIS ROBITAILLE,²¹ ARCHANA SOAM,²² MEHRNOOSH TAHANI,²³ XINDI TANG,²⁴
MOTOHIDE TAMURA,^{25,19,26} DAVID BERRY,²⁷ PIERRE BASTIEN,²⁸ TAO-CHUNG CHING,^{8,29} SIMON COUDÉ,²²
WOOJIN KWON,^{30,31} JIA-WEI WANG,¹⁰ TETSUO HASEGAWA,²⁵ SHIH-PING LAI,^{32,10} AND KEPING QIU^{33,34}

¹Jeremiah Horrocks Institute, University of Central Lancashire, Preston PR1 2HE, UK

²Centre for Astronomy, School of Physics, National University of Ireland Galway, University Road, Galway H91 TK33, Ireland

³NRC Herzberg Astronomy and Astrophysics, 5071 West Saanich Road, Victoria, BC V9E 2E7, Canada

⁴Department of Physics and Astronomy, University of Victoria, Victoria, BC V8W 2Y2, Canada

⁵Aix Marseille Univ., CNRS, CNES, LAM, Marseille, France

⁶Purple Mountain Observatory, Chinese Academy of Sciences, 10 Yuanhua, 210033 Nanjing, People's Republic of China

⁷Vietnam National Space Center, Vietnam Academy of Science and Technology, 18 Hoang Quoc Viet, Hanoi, Vietnam

⁸CAS Key Laboratory of FAST, National Astronomical Observatories, Chinese Academy of Sciences, Peoples Republic of China

⁹National Astronomical Observatories, Chinese Academy of Sciences, A20 Datun Road, Chaoyang District, Beijing 100012, Peoples Republic of China

¹⁰Academia Sinica Institute of Astronomy and Astrophysics, No.1, Sec. 4., Roosevelt Road, Taipei 10617, Taiwan

¹¹Tokushima University, Minami Jousanajima-machi 1-1, Tokushima 770-8502, Japan

¹²Institute of Liberal Arts and Sciences Tokushima University, Minami Jousanajima-machi 1-1, Tokushima 770-8502, Japan

¹³Korea Astronomy and Space Science Institute, 776 Daedeokdae-ro, Yuseong-gu, Daejeon 34055, Republic of Korea

¹⁴University of Science and Technology, Korea, 217 Gajeong-ro, Yuseong-gu, Daejeon 34113, Republic of Korea

¹⁵National Astronomical Observatory of Japan, Alonso de Córdova 3788, Office 61B, Vitacura, Santiago, Chile

¹⁶Joint ALMA Observatory, Alonso de Córdova 3107, Vitacura, Santiago, Chile

¹⁷NAOJ Fellow

¹⁸Department of Physics and Astronomy, University College London, WC1E 6BT London, UK

¹⁹Department of Astronomy, Graduate School of Science, The University of Tokyo, 7-3-1 Hongo, Bunkyo-ku, Tokyo 113-0033, Japan

²⁰Department of Physics, Faculty of Science and Engineering, Meisei University, 2-1-1 Hodokubo, Hino, Tokyo 191-8506, Japan

²¹Univ. Grenoble Alpes, CNRS, IPAG, 38000 Grenoble, France

²²SOFIA Science Center, Universities Space Research Association, NASA Ames Research Center, Moffett Field, California 94035, USA

²³Dominion Radio Astrophysical Observatory, Herzberg Astronomy and Astrophysics Research Centre, National Research Council Canada, P. O. Box 248, Penticton, BC V2A 6J9 Canada

²⁴Xinjiang Astronomical Observatory, Chinese Academy of Sciences, 830011 Urumqi, Peoples Republic of China

²⁵National Astronomical Observatory of Japan, National Institutes of Natural Sciences, Osawa, Mitaka, Tokyo 181-8588, Japan

²⁶Astrobiology Center, National Institutes of Natural Sciences, 2-21-1 Osawa, Mitaka, Tokyo 181-8588, Japan

²⁷East Asian Observatory, 660 N. A'ohōkū Place, University Park, Hilo, HI 96720, USA

²⁸Centre de recherche en astrophysique du Québec & département de physique, Université de Montréal, C.P. 6128 Succ. Centre-ville, Montréal, QC, H3C 3J7, Canada

²⁹National Astronomical Observatories, Chinese Academy of Sciences, A20 Datun Road, Chaoyang District, Beijing 100012, People's Republic of China

³⁰Department of Earth Science Education, Seoul National University, 1 Gwanak-ro, Gwanak-gu, Seoul 08826, Republic of Korea

³¹SNU Astronomy Research Center, Seoul National University, 1 Gwanak-ro, Gwanak-gu, Seoul 08826, Republic of Korea

³²Institute of Astronomy and Department of Physics, National Tsing Hua University, Hsinchu 30013, Taiwan

³³School of Astronomy and Space Science, Nanjing University, 163 Xianlin Avenue, Nanjing 210023, Peoples Republic of China

³⁴Key Laboratory of Modern Astronomy and Astrophysics (Nanjing University), Ministry of Education, Nanjing 210023, People's Republic of China

(Received March 9, 2021; Revised March 26, 2021; Accepted March 29, 2021)

ABSTRACT

We present the first $850\,\mu\text{m}$ polarization observations in the most active star-forming site of the Rosette Molecular Cloud (RMC, $d \sim 1.6\,\text{kpc}$) in the wall of the Rosette Nebula, imaged with the SCUBA-2/POL-2 instruments of the JCMT, as part of the B-Fields In Star-Forming Region Observations 2 (BISTRO-2) survey. From the POL-2 data we find that the polarization fraction decreases with the $850\,\mu\text{m}$ continuum intensity with $\alpha = 0.49 \pm 0.08$ in the $p \propto I^{-\alpha}$ relation, which suggests that some fraction of the dust grains remain aligned at high densities. The north of our $850\,\mu\text{m}$ image reveals a “gemstone ring” morphology, which is a $\sim 1\,\text{pc}$ -diameter ring-like structure with extended emission in the “head” to the south-west. We hypothesize that it might have been blown by feedback in its interior, while the B-field is parallel to its circumference in most places. In the south of our SCUBA-2 field the clumps are apparently connected with filaments which follow Infrared Dark Clouds (IRDCs). Here, the POL-2 magnetic field orientations appear bimodal with respect to the large-scale *Planck* field. The mass of our effective mapped area is $\sim 174\,M_{\odot}$ that we calculate from $850\,\mu\text{m}$ flux densities. We compare our results with masses from large-scale emission-subtracted *Herschel* $250\,\mu\text{m}$ data, and find agreement within 30%. We estimate the POS B-field strength in one typical subregion using the Davis-Chandrasekhar-Fermi (DCF) technique and find $80 \pm 30\,\mu\text{G}$ toward a clump and its outskirts. The estimated mass-to-flux ratio of $\lambda = 2.3 \pm 1.0$ suggests that the B-field is not sufficiently strong to prevent gravitational collapse in this subregion.

Keywords: ISM: clouds — ISM: individual objects (RMC) — ISM: magnetic fields — submillimeter: ISM — stars: formation — techniques: polarimetric

1. INTRODUCTION

The role of the magnetic field (B-field) through the evolutionary stages of star formation from the scale of molecular clouds down to the scale of protostars is crucial to our understanding of the star formation process. In particular, it is not well understood whether B-fields help or hinder star formation at each stage and on different spatial scales (Hull & Zhang 2019, and references therein)

Submillimeter continuum polarization surveys have the potential to allow us to trace dust properties and the orientation of the plane-of-sky B-field in molecular clouds (e.g., Matthews et al. 2009). The polarization data, when complemented with molecular line information, are also a powerful tool for estimating the magnetic field strength using the Davis-Chandrasekhar-Fermi method (Davis 1951; Chandrasekhar & Fermi 1953). The JCMT Large Program BISTRO surveys are using the SCUBA-2 bolometer array with its associated POL-2 polarimeter, to survey numerous star formation regions (Ward-Thompson et al. 2017). The resolution of these surveys ($\sim 14''$ at $850\,\mu\text{m}$) is intermediate between the large-scale, low-resolution ($\sim 5'$) *Planck* survey (e.g., Planck Collaboration XXXV et al. 2016) and the very high-resolution ($\sim 0.5''$) small-scale observations of interferometers such as ALMA (e.g., Pattle et al. 2020b).

The original BISTRO-1 program (Ward-Thompson et al. 2017) aimed to produce an unbiased survey of the magnetic field in a large sample of typically low-mass star-forming regions in the solar neighborhood.

The subsequent BISTRO-2 survey now aims to explore the ‘mass axis’ of star formation parameter space by targeting intermediate- and high-mass star-forming regions out to a distance of $\sim 2\,\text{kpc}$. The BISTRO-1 and 2 programs have generated a homogeneous, statistically significant sample of legacy observations, with which we are investigating how the behaviour of magnetic fields changes from low-mass to high-mass star formation, hence allowing us to study the interplay between self-gravity of the gas and other forces.

In this paper we present the first BISTRO-2 results in the high-mass star-forming center of the Rosette Molecular Cloud (RMC). The RMC looks just as a “petal” of the Rosette Nebula the cavity of which appears to have been blown by the central OB cluster NGC 2244 and its expanding HII-region (see left panel of Fig. 1), which interacts with the cloud (Román-Zúñiga & Lada 2008). This prominent nebula is located in the larger Monoceros OB2 cloud (see Pérez 1991), in the constellation Monoceros.

Distance estimates to NGC 2244 range from 1.4 to 1.7 kpc (Ogura & Ishida 1981; Perez et al. 1987; Hensberge et al. 2000; Park & Sung 2002; Lombardi et al. 2011; Martins et al. 2012; Bell et al. 2013; Kharchenko et al. 2013). Gaia DR2 yields a distance estimate to NGC 2244 of 1.59 kpc with a 1% statistical error and an 11% systematic error (Mužić et al. 2019). In this work, therefore, we adopt $\sim 1.6\,\text{kpc}$ as the distance of the RMC. The stellar content of the cluster has been extensively studied from X-ray to mid-infrared wave-

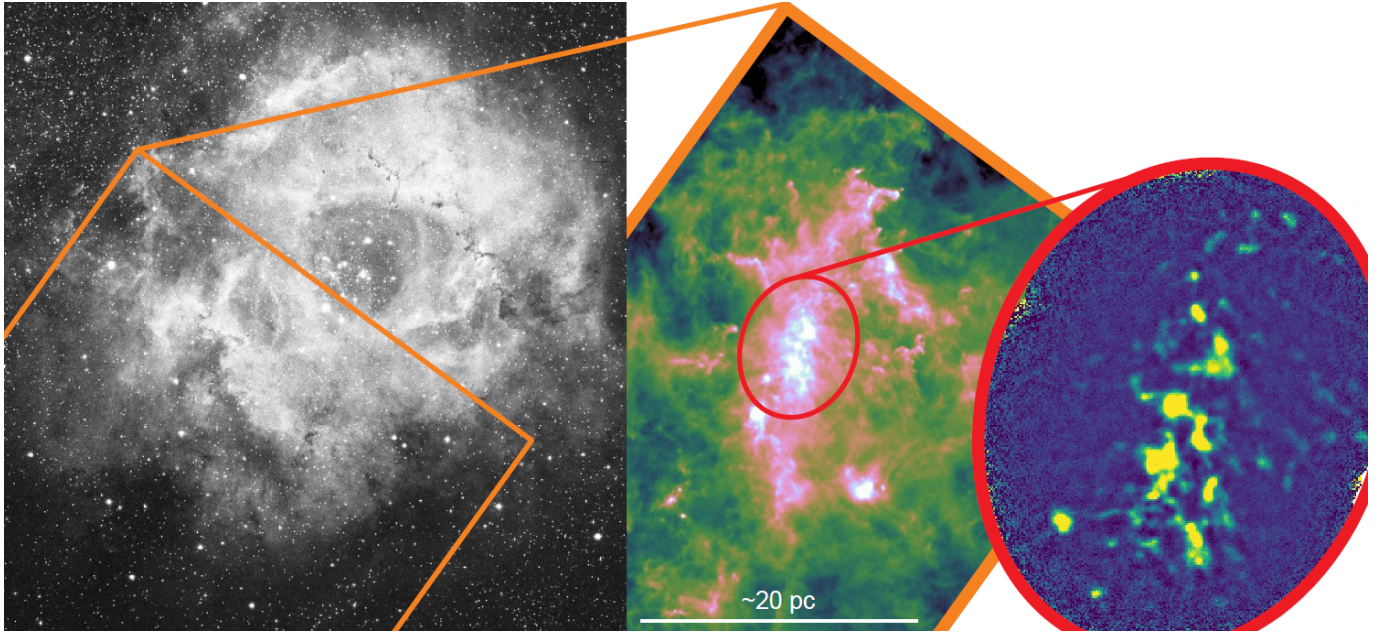


Figure 1. The left panel shows the Rosette Nebula in an optical map from the all-sky Digital Sky Survey (Lasker et al. 1990). The RMC portion of the nebula is shown as a $250\,\mu\text{m}$ *Herschel* image (e.g., Schneider et al. 2010) in the middle panel. The zoomed image on the right displays the Stokes I image from our new data of the most active star-forming center of the RMC ($d \sim 1.6\,\text{kpc}$) observed by SCUBA-2/POL-2 on JCMT (see Fig. 2).

lengths. Seven main O-stars are thought to be evacuating the central part of the nebula as part of the ionizing cluster NGC 2244 (Martins et al. 2012), the closest of which (only in projection), HD 46485, is marked in Fig. 2. The cluster’s young age, $\sim 2\,\text{Myr}$ (e.g., Park & Sung 2002; Bell et al. 2013), together with the absence of non-thermal radio emission, lead to the conclusion that no supernova explosion has occurred yet in the nebula (Townesley et al. 2003).

Many embedded clusters have been identified in the RMC. Seven of them (PL01-07) were found by Phelps & Lada (1997) at near-infrared (NIR) wavelengths. Román-Zúñiga et al. (2008) discovered two more NIR clusters, REFL08 and REFL09. Poulton et al. (2008) defined clusters with IR excess sources from A to G, extending from a few to several square parsecs. The center of the RMC, that we observed with JCMT, contains most of the cluster members of PL04a/b, PL05, and REFL08, which are associated with a single CO clump identified by Williams et al. (1995). The cluster E identified by Poulton et al. (2008) covers most of our observed region except PL04a/b and PL05 (see their Figure 10.). In PL04a (see Fig. 2) near-infrared-excess sources coincide spatially with the NIR nebulosity (Román-Zúñiga et al. 2008). Around PL04b, X-ray sources have been found with *Chandra* by Wang et al. (2009), which indicate the presence of Class III young stellar objects (YSOs).

Román-Zúñiga et al. (2008) estimated that the gas-rich clusters of the RMC center provide half of the star formation in the whole cloud. This subregion is beyond the ionization front of the HII region where a shock front may have already passed through. From their NIR survey they found that the age of the cluster members decreases with increasing distance from the Rosette Nebula. Román-Zúñiga et al. (2008) hypothesised that the origin of the age sequence with small age differences is primordial, a result of the formation and evolution of the cloud, and not of the HII region. This result has been confirmed by Poulton et al. (2008), Ybarra et al. (2013), and Cambrésy et al. (2013). Based on near-infrared JHK_s and WISE data, Cambrésy et al. (2013) also find that the age distribution of the young clusters in the region is not consistent with a triggered star formation scenario, and they conclude that the evolution of the Rosette complex is not governed by the influence of the central OB star population. Interestingly, the cloud collapse may have been triggered externally which then formed the dense ridge, located along the mid-plane of the cloud (see the middle panel of Fig. 1), and ignited star formation (Poulton et al. 2008).

Far-infrared and submillimeter *Herschel* HOBYS data (Motte et al. 2010) of the Rosette region also shed light on the influence of NGC 2244 on the cloud (Schneider et al. 2010; Tremblin et al. 2013, 2014). The authors present the properties of embedded protostellar sources

(Hennemann et al. 2010), and assess the clump populations up to 1 pc in size (di Francesco et al. 2010). From the distribution of starless and protostellar clumps, the latter authors did not find an age-gradient across the RMC. However, Schneider et al. (2010) tentatively conclude from the spatial distribution of the most massive dense cores ($0.05 - 0.3$ pc) that there may be an age sequence with younger cores further away from NGC 2244 that is consistent with the above findings of Poulton et al. (2008), Román-Zúñiga et al. (2008), Ybarra et al. (2013), and Cambrésy et al. (2013). Schneider et al. (2012) investigate the filamentary structure of the RMC and propose that the sites of star-cluster formation correlate with the junctions of the filamentary network. For part of the *Herschel* coverage in Rosette, see the middle panel of Fig. 1.

Planck Collaboration XXXIV et al. (2016) traced the 3D magnetic field structure of Rosette with *Planck* polarization data combined with rotation measure (RM) observations from Savage et al. (2013) to trace the magnetic field at low resolution both in the molecular and ionized parts of the cloud. The analytical model of Planck Collaboration XXXIV et al. (2016) reproduced the large-scale mean observed properties in the Rosette, such as the rotation measure distribution and mean dust polarization values.

These *Planck* observations show that the large-scale magnetic field in the Rosette’s parent molecular cloud is mostly parallel to the large-scale field along the Galactic plane. Planck Collaboration XXXIV et al. (2016) found overall low polarization fractions in and around the Rosette Nebula, typically $p < 6\%$, with the lowest values ($p \lesssim 3\%$) toward the densest regions. They estimate a line-of-sight (LOS) B-field strength of $\sim 3 \mu\text{G}$ from rotation measure data. The strength and structure of the magnetic field in Rosette was also estimated by Costa et al. (2016) from Faraday rotation measurements of extragalactic radio sources through the nebula. In agreement with earlier results, they also detect an excess rotation measure at the shell of the Rosette Nebula.

We present here the first results from the BISTRO-2 survey of the actively star-forming RMC center. The paper is organized as follows. Section 2 provides details about the JCMT observations and the data reduction. In Section 3 we present the polarization properties, and the magnetic field morphology. In Section 4 we derive and discuss the mass of the region, and the B-field strength with DCF analysis. Finally, Section 5 presents our main conclusions.

2. OBSERVATIONS AND DATA REDUCTION

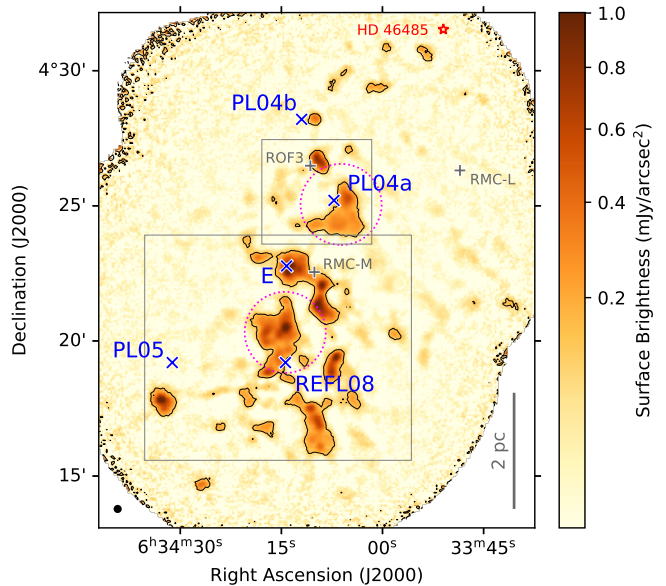


Figure 2. Stokes I image of the RMC at $850 \mu\text{m}$, the FWHM resolution of which is $\sim 14''$. The beam is shown in the lower left corner. Dotted magenta circles show the central $3'$ -diameter regions, and the black contours correspond to $10\sigma_I = 0.13 \text{ mJy/arcsec}^2$. In the following we display results in the outlined boxes. Projected center positions of NIR clusters are marked with blue crosses (PL, REFL, and E indicate cluster positions identified by Phelps & Lada (1997); Román-Zúñiga et al. (2008), and Poulton et al. (2008), respectively). The RMC-M and RMC-L sources marked in gray are possible [SII] outflow features from Ybarra & Phelps (2004), and ROF3 is a CO outflow feature found by Dent et al. (2009). The red star shows the position of the closest O-star of NGC 2244 (in projection).

As part of the JCMT BISTRO-2 survey, the central part of the Rosette molecular cloud was observed at $850 \mu\text{m}$ with SCUBA-2 (Holland et al. 2013) and POL-2 (Friberg et al. 2016) between 12 January 2019 and 02 May 2019, under JCMT project code M17BL011. The region was observed in two overlapping tiles, each was observed 20 times for ~ 40 minutes each time, giving a total on-source integration time of ~ 27 hours. The two overlapping observations were made with the POL-2 DAISY mode (Friberg et al. 2016), which produces a map with high signal-to-noise ratio (SNR) in the central $3'$ -diameter region with increasing noise to the edges. These were combined during the data reduction with the ‘multi-object’ keyword on. Bad datasets were not found among the observations. During the observations the atmospheric opacity, τ at 225 GHz, varied between ~ 0.02 and ~ 0.07 .

The effective beam size of JCMT is $14.1''$ (~ 0.1 pc at 1.6 kpc) at $850 \mu\text{m}$. Continuum polarimetric observa-

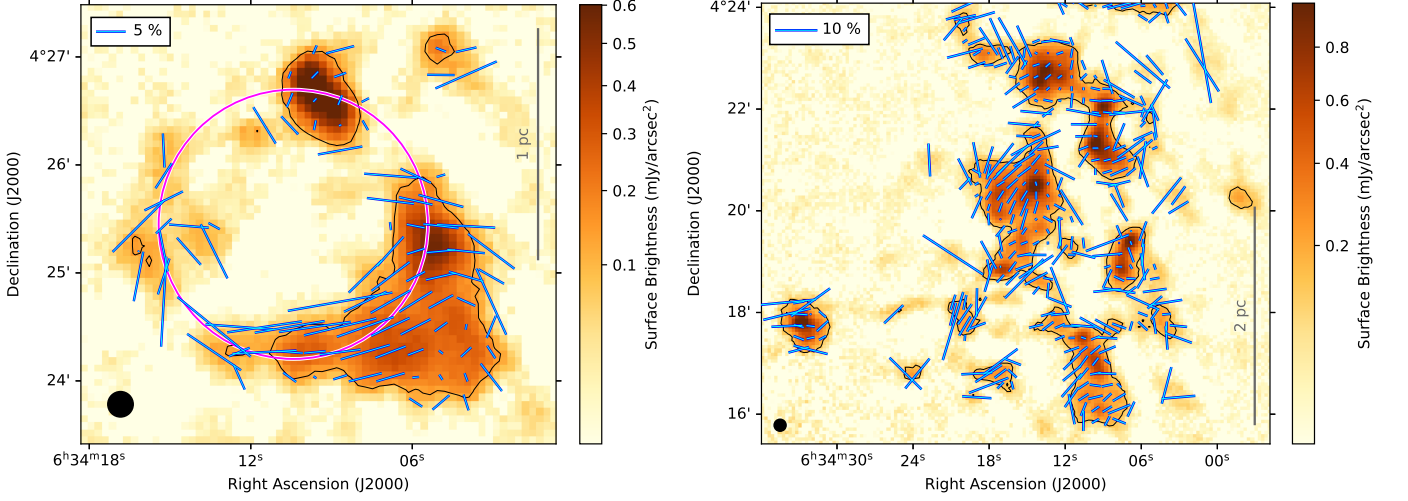


Figure 3. Maps of debiased polarization half-vectors in the central part of the RMC, coarsely selected with the criteria of $I > 0$, $I/\delta I > 10$, and $\delta p < 5\%$. The lengths of the POL-2 half-vectors in blue are proportional to their polarization fractions, the scale of which is shown in the map panels. The background is a SCUBA-2 $850\,\mu\text{m}$ Stokes I image, where the black contours are as in Fig. 2. **Left:** Polarization map of the northern field, featuring the ring-like structure that is indicated by the magenta circle (see Fig. 2). **Right:** Polarization map of the southern field (also see Fig. 2).

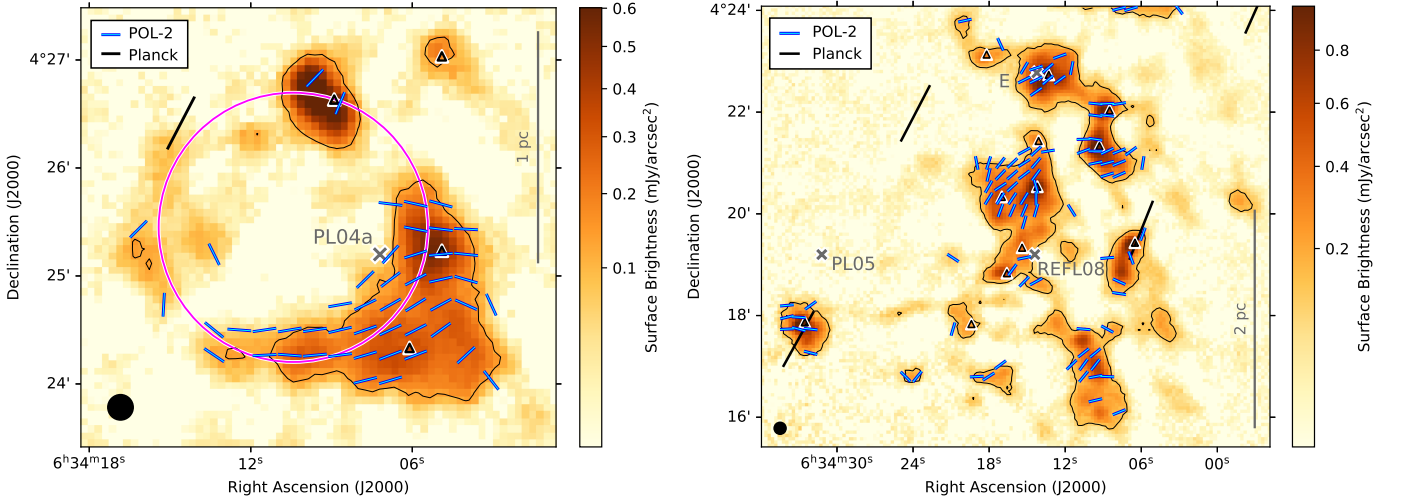


Figure 4. Maps of polarization half-vectors, rotated by 90° to show the orientation of the B-field, selected with the criteria of $I > 0$, $I/\delta I > 10$, $p/\delta p > 3$, and $\delta p < 5\%$ (see Sect. 3.1). The POL-2 magnetic half-vectors in blue have equal lengths in each panel, and are plotted on a $14''$ vector grid. Planck B-field-oriented vectors (on a $5'$ -scale) are shown in black, which are approximately parallel to the Galactic plane, as found by Planck Collaboration XXXIV et al. (2016). The background is a SCUBA-2 $850\,\mu\text{m}$ Stokes I image, where the black contours are as in Fig. 2. Triangle symbols mark the submillimeter-continuum objects detected by SCUBA (Di Francesco et al. 2008). **Left:** Magnetic-field vector map of the northern field, featuring the ring-like structure of PL04a, indicated by the magenta circle (see Fig. 2 and text). **Right:** Magnetic-field vector map of the southern field (also see Fig. 2).

tions were simultaneously taken at $450\,\mu\text{m}$ with a resolution of $9.6''$, although those data will be presented in a future publication; and in this paper we only discuss the $850\,\mu\text{m}$ dataset.

The $850\,\mu\text{m}$ data were reduced using the SMURF (Jenness et al. 2013; Berry et al. 2005) package in Starlink (Currie et al. 2014). In short, the *calcqu* command of the SMURF package was used first to convert the raw bolometer data into Stokes I , Q , and U time-

streams. Then, all the time-streams of the observations were co-added into a first solution Stokes I map with the *makemap* routine inside the *pol2map* script of the SMURF package. Re-running this task creates the final improved I map from the first I map solution (Jenness et al. 2013; Berry et al. 2005). Finally, *makemap* is also used for creating the Q and U maps from their time-streams, along with their variance maps, and the polarization half-vector catalog (Mairs et al. 2015; Pattle et al. 2017). The term ‘half-vector’ is used because of the $\pm 180^\circ$ ambiguity in the inferred magnetic field direction (e.g., Kirk et al. 2006; Pattle et al. 2017) – i.e., we do not know which end of the half-vector to put the ‘arrow’ on. The final improved Stokes I map, adopting the “January 2018” instrumental polarization model (Friberg et al. 2018), was used to help correct for the instrumental polarization in the Q and U maps.

The final Stokes I , Q , U maps and the polarization catalog are gridded to a default $4''$ /pixel scale. In these maps we estimated the one-sigma sensitivities σ_I , σ_Q , σ_U to be 2.9, 2.4, and 2.2 mJy/beam, respectively. The corresponding uncertainties in the respective order are 0.013, 0.011, and 0.010 in mJy/arcsec², and the level of $10\sigma_I = 0.13$ mJy/arcsec² is marked in our Stokes I figures.

With the *pol2map* binsize parameter we generated a catalog of independent polarization vectors binned to a $14''$ /pixel scale (to match the beam size), while for the Stokes I map we use at the default $4''$ /pixel scale (to produce a smoother-looking image). The data acquisition and reduction, as well as the absolute calibration of the data are discussed in detail by Ward-Thompson et al. (2017).

3. RESULTS AND ANALYSIS

3.1. Polarization properties

The BISTRO-2 observations with SCUBA-2 and POL-2 cover the most active star-forming site in the wall of the Rosette Nebula within an effective area of ~ 0.06 square degrees, or ~ 45 pc² at a distance of ~ 1.6 kpc. See Fig. 1 for a large view of the Rosette Nebula, and Fig. 2 for the $850\ \mu\text{m}$ Stokes I map toward the center of the RMC made with SCUBA-2.

We follow the conventional definitions of the polarization properties (e.g., Pattle et al. 2017; Coudé et al. 2019). The measured polarization angles are defined as $\theta = 0.5 \arctan(U/Q)$. The non-debiased polarized intensity is $I_p = (Q^2 + U^2)^{0.5}$, and the corresponding polarization fraction is defined as $p = I_p/I$. The debiased polarized intensity, however, is calculated as $I_p^{\text{db}} = (Q^2 + U^2 - 0.5[(\delta Q)^2 + (\delta U)^2])^{0.5}$, with $\delta Q = \sqrt{V_Q}$ and $\delta U = \sqrt{V_U}$, where V_Q and V_U are the variances

of Q and U . The debiased polarization fraction is then given as $p^{\text{db}} = I_p^{\text{db}}/I$.

In Fig. 3, we show a more complete set of our polarization data that we coarsely selected with the criteria of Stokes $I > 0$, $I/\delta I > 10$, and $\delta p < 5\%$. Here, the debiased polarization half-vectors also preserve the information on the percentage polarization. The polarization vector field seems ordered in the higher Stokes I – and a priori denser – regions, and the polarization fraction appears to decrease with increasing density (see Sect. 3.2).

However, for most of the following analysis, we use the vector selection criteria of Stokes $I > 0$, $I/\delta I > 10$, $p^{\text{db}}/\delta p > 3$, and $\delta p < 5\%$, where δI and δp indicate the uncertainty in total intensity and polarization fraction (both non-debiased and debiased), respectively. This set of independent criteria, giving us 152 vectors at $14''$ binning, were adapted from the criteria used in, for example, Coudé et al. (2019).

We consider polarization half-vectors rotated by 90° to trace the magnetic field direction that we refer to as “magnetic field half-vectors” in the plane of the sky. This can be assumed, however, only if the dust grain size is much smaller than the observed wavelength (Kirchschlager et al. 2019; Guillet et al. 2020). Then, the emitting elongated dust grains are mostly aligned by the magnetic field, and the magnetic field direction is orthogonal to the polarization direction (e.g., Lazarian & Hoang 2007; Hoang & Lazarian 2016).

The above-selected POL-2 magnetic half-vectors in the plane-of-sky (POS) are shown in Fig. 4, overlaid on our Stokes I map.

3.2. $p - I$ relationship

Dust grain alignment efficiency can be assessed using the relationship between polarization efficiency and visual extinction (e.g., Whittet et al. 2008; Jones et al. 2015). For optically thin submillimeter emission polarimetry, this is commonly treated as a relationship between the polarization fraction and total intensity (e.g., Jones et al. 2015). Observations of polarized dust emission typically show a power-law dependence, $p \propto I^{-\alpha}$, where $0 \leq \alpha \leq 1$. A steeper index (higher α) indicates poorer grain alignment; $\alpha = 0$ indicates that grains are equally well aligned at all depths, while $\alpha = 1$ indicates either a lack of aligned grains, or that all observed polarized emission is produced in a thin layer at the cloud’s surface (Pattle et al. 2019, and references therein).

In order to avoid selection biases which may influence these relationships, we infer dust grain alignment properties from Ricean statistics. We measured α using the method described by Pattle et al. (2019), in which we

assume that the underlying relationship between *non-debiased* p and I can be parameterized as

$$p = p_{\sigma_{QU}} \left(\frac{I}{\sigma_{QU}} \right)^{-\alpha} \quad (1)$$

where $p_{\sigma_{QU}}$ is the polarization fraction at the RMS noise level of the data σ_{QU} , and α is a power-law index in the range $0 \leq \alpha \leq 1$. We fitted the relationship between I and observed polarization fraction p' with the mean of the Ricean distribution of observed values of p which would arise from Eq. 1 in the presence of Gaussian RMS noise σ_{QU} in Stokes Q and U :

$$p'(I) = \sqrt{\frac{\pi}{2}} \left(\frac{I}{\sigma_{QU}} \right)^{-1} \mathcal{L}_{\frac{1}{2}} \left(-\frac{p_{\sigma_{QU}}^2}{2} \left(\frac{I}{\sigma_{QU}} \right)^{2(1-\alpha)} \right), \quad (2)$$

where $\mathcal{L}_{\frac{1}{2}}$ is a Laguerre polynomial of order $\frac{1}{2}$. See [Pat-
tle et al. \(2019\)](#) for a derivation of this result. We re-
stricted our dataset to the central 3-arcminute diame-
ter region around each pointing centre over which ex-
posure time, and so RMS noise, is approximately con-
stant ([Friberg et al. 2016](#)). We estimated an RMS noise
value in our Stokes Q and U data of 0.62 mJy/beam
on 12'' pixels, and $p_{\sigma_{QU}} = 0.36 \pm 0.14$ for polarization
fraction at this noise level.

Figure 5 shows the $p - I$ relationship in the cen-
tral ridge of the RMC, and for the central regions of
our observed field. We measure a best-fit index of
 $\alpha = 0.49 \pm 0.08$, i.e., $p \propto I^{-0.49 \pm 0.08}$. This suggests
that in the RMC, dust grain alignment efficiency de-
creases approximately linearly with increasing density
(cf., [Jones et al. 2015](#)), but that some fraction of the
grains remain aligned with respect to the magnetic field
to highest densities. The partially aligned nature of the
dust grains at high densities is also supported by the
strongly correlated position angles of the polarization
half-vectors which we observe (see Fig. 3).

3.3. Magnetic Field Morphology

We obtained the POS magnetic field half-vectors by
rotating the polarization half-vectors by 90° . The mag-
netic field orientations with equal length vectors are
shown in Fig. 4 in the northern and southern map por-
tions which cover most of the 850 μm emission in the
central ridge of the RMC.

In the following, based on Stokes I and associated
data, we describe a ring-like structure in the northern
part of the observed field, and the system of clumps
and elongated features in the observed south. We refer
to their positions mainly with respect to the projected
centers of NIR clusters listed in Sect. 1.

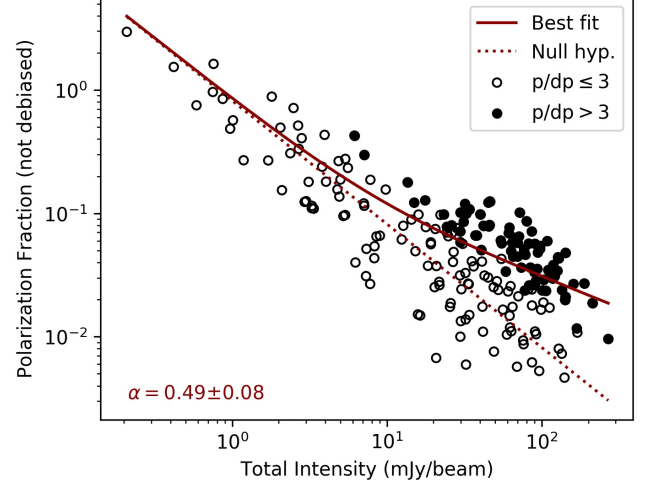


Figure 5. Non-debiased polarization fraction p as a function of total intensity at 850 μm fitted with the mean of the Ricean distribution of p . All of the data points above $I = 0$ were fitted within the central 3'-diameter regions of the combined map (see Fig. 2), the $p/\delta p > 3$ points (filled circles) are marked for information. The red solid line gives the best-fit model with $\alpha = 0.49 \pm 0.08$, and the dashed line shows the null hypothesis; the expected behavior of non-aligned dust grains.

3.3.1. A ring seen by SCUBA-2

In the north of the region, around PL04a, the 850 μm emission reveals a ring-like structure with a diameter of ~ 1 pc. It is traced by a dense clump in the north of the ring, weaker emission in the east, and strong clumpy emission extending away from the ring in the south-west. This latter corner looks just as a “gemstone head of a ring with side stones” (see the left panel of Fig. 4).

The B-field seems to trace the circumference of the ring in the south and weakly in the east (where we have sufficient signal-to-noise ratio to plot vectors. However, see Fig. 3/left for more polarization vectors along the ring). In the western part of the ring, where there is a slightly brighter clump, the B-field appears to run almost perpendicular to the circumference; a similar pattern is seen in the north, but there it is based on low numbers of half-vectors. The pattern around the “gemstone” head is less clear because, again, we appear to have insufficient signal-to-noise ratio to plot sufficient number of half-vectors.

This ring morphology that we see in our Stokes I image, is also visible at shorter wavelengths. The *Spitzer* IRAC/MIPS data from 3.6 μm to 24 μm reveal emission around a cluster of stars at the western/south-western position along the ring (see the bright cyan sources in Fig. 6, and the *Spitzer*-only image in Figure 2 of [Poulton](#)

et al. (2008)). At these bright sources, 2MASS (Cutri et al. 2003), WISE (Cutri & et al. 2012; Cambr sy et al. 2013), and other IR (Bica et al. 2003; Phelps & Lada 1997) star clusters are registered, with (candidate) YSOs around. For the distribution of YSOs in our whole observed field, see Fig 7.

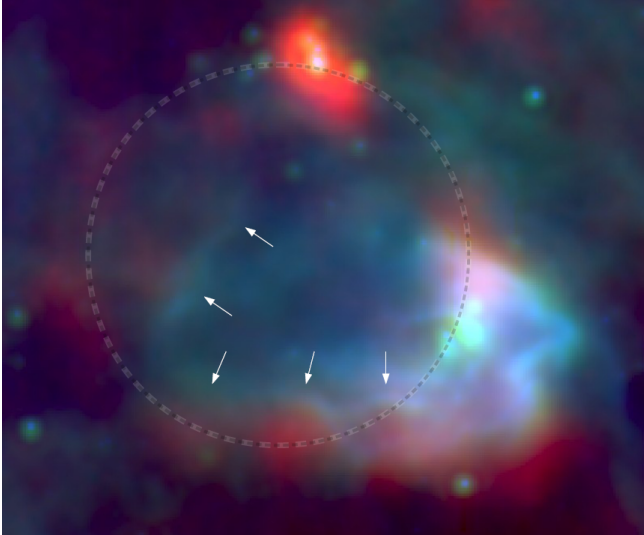


Figure 6. RGB composite image of the SCUBA-2 “gemstone ring”, where $850\,\mu\text{m}$ emission of cold dust is red, $24\,\mu\text{m}$ hot dust emission is green, and the $8\,\mu\text{m}$ PAH emission is blue. The overplotted ring is the same as in Fig. 4/left, and the arrows show where the short-wavelength emission seems to interact with the $850\,\mu\text{m}$ emission of the dense clumps (see text for details).

The short-wavelength emission of the YSO cluster seems to illuminate and fill the interior of our ring. We have marked with arrows in Fig. 6 where it appears that the *Spitzer* emission ($8\,\mu\text{m}$ – blue, $24\,\mu\text{m}$ – green) is in direct interaction with the $850\,\mu\text{m}$ (red) clumps. The arc-shaped red-green-blue gradients along the arrows probably show us the penetration of the short-wavelength emission from the illuminating cluster sources (in the south-west of the ring) into the dense cloud material.

We speculate that this process might have shaped the $850\,\mu\text{m}$ dense material not only at the “gemstone” and “side stones”, but in a large part of the ring. The short-wavelength bow-shock-shaped emission (in cyan in Fig. 6) may be due to a break out of the clumpy ring/bubble toward the west and toward the observer (see Fig. 4/left and Fig. 6). However, this hypothesis needs to be further investigated.

HII regions can be identified using mid-infrared (MIR) wavelengths as well. Galactic HII regions are typically characterized by a rim-like $\sim 10\,\mu\text{m}$ emission surrounding bubble-like radiation at $\sim 20\,\mu\text{m}$ that coincide with

the ionized gas. (e.g., Povich et al. 2007; Anderson et al. 2011; Simpson et al. 2012).

The $\sim 10 - 20\,\mu\text{m}$ emission is from polycyclic aromatic hydrocarbon (PAH) molecules which fluoresce in the presence of ultraviolet radiation fields, and can thus be identified in $8\,\mu\text{m}$ and $24\,\mu\text{m}$ images. Fig. 6 shows similar “layered” MIR features in an $850\,\mu\text{m}$ ring-like structure, and Fig 7 shows the distribution of the $8\,\mu\text{m}$ emission on a larger scale.

The ring itself looks like a cavity blown by feedback in its interior, and the B-field is parallel to the circumference of the arc in most places. Similar “curved” magnetic field geometry was found in the ring-like shell of bubble N4 by Chen et al. (2017) from NIR polarization. In their Radiation MHD simulations of HII regions, Arthur et al. (2011) also witness mostly parallel orientations of the magnetic fields to the shell and ionisation front.

We also note that the H_2 column density values (Ladell et al., in prep.) in the whole observed region are everywhere above the inferred threshold of $\log_{10}(N_{\text{H}}) \approx 21.7\,\text{cm}^{-2}$ (or $\sim 2.5 \times 10^{21}\,\text{cm}^{-2}$ in N_{H_2}) where the preferred relative orientation between the B-field and density structures change from parallel to perpendicular (Planck Collaboration XXXV et al. 2016). Therefore, neither in the ring, nor in the observed field can we test this *Planck* threshold.

3.3.2. The southern field

In the southern part of the RMC center, Dec(2000) $\lesssim 4^\circ 24'$ in Fig. 2, the SCUBA-2 field looks clumpy. This can also be seen in the right panel of Fig. 4, overplotted with the submillimeter-continuum objects detected by SCUBA (Di Francesco et al. 2008). Some of the SCUBA/SCUBA-2 clumps seem to be connected with each other by $850\,\mu\text{m}$ emission filamentary features.

Here, the selected POL-2 magnetic half-vectors appear to be ordered at higher $850\,\mu\text{m}$ emission and they roughly follow the *Planck* B-field in the following areas: at the center position of cluster E; between cluster E and REFL08; and south-west of REFL08. Our B-field seems to turn roughly east-west in the other two clumps (south of PL05, and south-west of cluster E). So, the field geometry appears bimodal with some clumps well aligned with the large-scale field and some clumps nearly perpendicular.

Most of the clumpy and elongated $850\,\mu\text{m}$ features seem to lie along emission at IRAC/MIPS wavelengths which look like infrared dark clouds (IRDCs). For a combined image of $3.6 - 4.5 - 5.8\,\mu\text{m}$ and at $24\,\mu\text{m}$ see this approximate subregion in Figure 10 of Poulton et al. (2008), and our Fig 7 for the $8\,\mu\text{m}$ coverage.

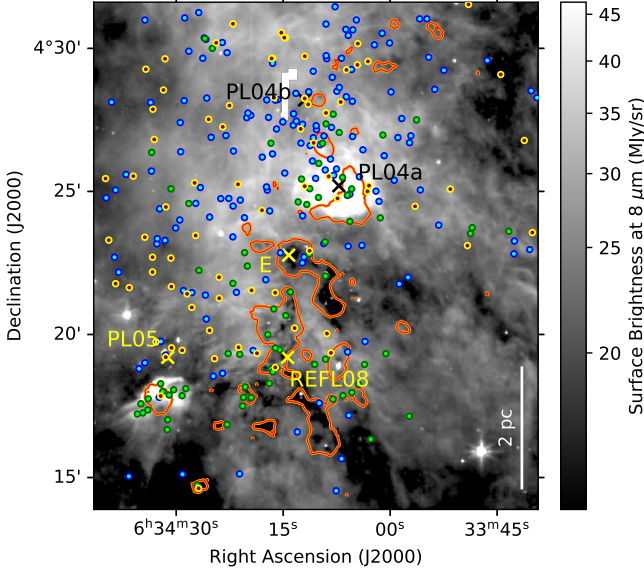


Figure 7. *Spitzer*/IRAC $8\mu\text{m}$ emission shown by the grayscale image with $10\sigma_I$ $850\mu\text{m}$ contours in red. The positions of (candidate) YSOs are overplotted in blue (2MASS: Cutri et al. 2003) and green (WISE: Cambr  sy et al. 2013). YSOs detected in X-ray by Chandra are overplotted in yellow/red (Wang et al. 2009; Broos et al. 2013).

In Figure 7 the $10\sigma_I$ $850\mu\text{m}$ contours correlate well with lower $8\mu\text{m}$ surface brightness around the cluster positions E and REFL08. It appears that there are fewer YSOs in the SCUBA-2 contours with the darkest $8\mu\text{m}$ emission, however for the positions and physical properties of the earlier stages of dense star-forming cores and protostars, using *Herschel*/HOBYS data, see Bontemps et al. (in prep.).

4. DISCUSSION

4.1. Dust masses

The total mass of a region is one indicator of its potential for star formation. Submillimeter flux densities are routinely used to estimate molecular cloud masses using the following formula:

$$M = \frac{d^2 F_\nu}{\kappa_\nu B_\nu(T_d)}, \quad (3)$$

where d (1600 pc) is the distance to the RMC, F_ν is the total flux density at $850\mu\text{m}$, κ_ν is the dust mass opacity, and $B_\nu(T_d)$ is the Planck function at dust temperature T_d .

We follow other BISTRO papers and the method of Beckwith et al. (1990) and formulate κ_ν as $0.1(\nu/\text{THz})^\beta \text{ cm}^2 \text{ g}^{-1}$, assuming a standard dust-to-gas ratio of 1:100. The dust emissivity index, β , has been

fixed to 2 (e.g., Hildebrand 1983; Roy et al. 2014; Pattle et al. 2015).

Within our mapped field ($\sim 12.9' \times 16.1'$, or $\sim 6 \times 7.5 \text{ pc}$), which is the whole region in Fig. 8, we derive a mass of $\sim 174 M_\odot$ for the RMC center. This mass includes $\sim 15 M_\odot$ for the ring region, and $\sim 84 M_\odot$ for the southern field, both estimated within their boxes outlined in Fig. 2. Within the region in the Stokes I image where $I/\delta I > 10$ (see the contours, for example, in Figs. 2 and 8), the mass corresponds to $\sim 41 M_\odot$.

For these masses we used a median T_d for each field that we estimated from the *Herschel* dust temperature image (see below, and also Ladjelate et al., in prep.). Assuming a typical factor of 2 uncertainty on the mass, we claim that there may be a few hundred solar masses of material in the densest regions probed by the JCMT.

Looking at our mapped field in *Herschel*/HOBYS H_2 column density data (Ladjelate et al., in prep.), the total mass was derived as in, for example, K  nyves et al. (2015, 2020) and resulted in $\sim 9.4 \times 10^3 M_\odot$. This *Herschel*-mass is about 2.5-times as much as that of the dense molecular gas material available in Orion B (K  nyves et al. 2020), in which low- to high-mass star formation is also occurring. At the same time, it represents only about 7% of the total mass of the whole Rosette Molecular Cloud region seen by *Herschel* (see this coverage in Fig. 1).

In order to make a comparison between a ground-based instrument, such as SCUBA-2, and a satellite, such as *Herschel*, it is necessary to take account of the very extended surface brightness seen by *Herschel*, to which SCUBA-2 is insensitive. To make such a comparison between our SCUBA-2 masses and *Herschel* masses we have taken the *Herschel* $250\mu\text{m}$ data which have a similar resolution ($18.2''$) to the SCUBA-2 data. In our effective mapped area we have selected a relatively empty $\sim 2'$ -diameter region, where we measured the median surface brightness in the $250\mu\text{m}$ map and used this offset to subtract the large-scale emission from the latter map. When we measure the remaining flux density at $250\mu\text{m}$ within our field (see the whole region in Fig. 8) and use Eq. 3, we obtain a mass of $\sim 238 M_\odot$. This shows good agreement (within 30%) with the mass we derived from SCUBA-2, above.

We note, however, that SCUBA-2's spatial filtering is more complicated than removing a zero-level offset; with different amounts of emission levels being removed at different scales up to $5'$. In addition, the choice of the dust emissivity index, β , or the dust opacity, κ_ν , may also adjust the result of this comparison.

The brightest $850\mu\text{m}$ emission pixels can be found in the clump south of PL05 (see e.g., Fig. 2), where the cor-

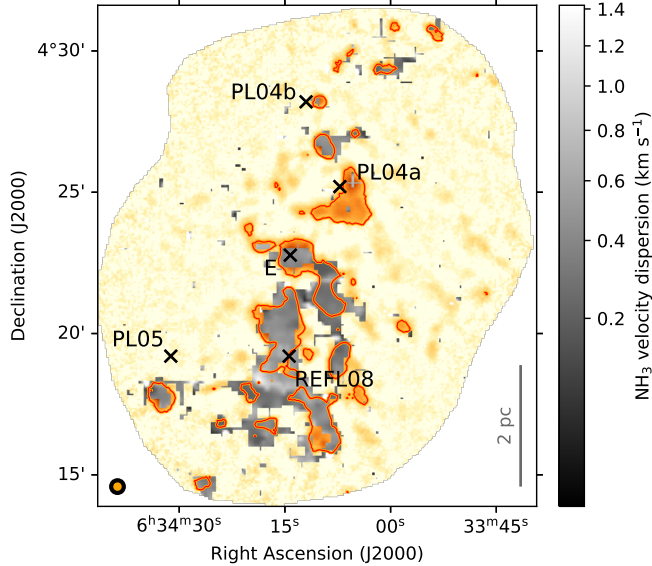


Figure 8. Background image is our 850 μm Stokes I map, with red contours at $10\sigma_I = 0.13 \text{ mJy/arcsec}^2$. In grayscale the $\text{NH}_3(1,1)$ velocity dispersions are overplotted from the KEYSTONE Survey (Keown et al. 2019). In the lower left corner the spatial resolutions of the JCMT 850 μm ($\sim 14''$) and the ammonia data ($32''$) are marked as orange and black circles, respectively.

responding average dust temperature and column densities give 18 K, and $N_{\text{H}_2} \sim 2.3 \times 10^{22} \text{ cm}^{-2}$, respectively. Apart from this, the one other ‘hot-spot’ in our image is the gemstone head of the ring with $T \sim 19 \text{ K}$. These two warmer spots correlate with locations of stronger 8 μm emission (see Fig. 7), and have somewhat lower column density than the colder (15 – 16 K) southern filamentary clumps. Indeed, colder areas tend to have higher column densities, where the absence of thermal heating and pressure support allow the matter to become more compact and eventually collapse into stars. For a comparison of the distribution of our “a priori” cold and dense 850 μm emission and the hot 8 μm PAH emission, see Fig. 7.

4.2. Magnetic Field Strength and Stability

The most commonly used method to infer the field strength from polarized dust emission is the Davis-Chandrasekhar-Fermi (DCF) technique (Davis 1951; Chandrasekhar & Fermi 1953) – see also work by Houde et al. (2016) and Pattle et al. (2017), and the discussion of its caveats and limitations in Pattle & Fissel (2019, and references therein). This method estimates the B-field strength by comparing the dispersion in the polarization orientation (assumed to be a measure of the non-uniform B-field) with the dispersion in LOS velocity (as-

sumed to be a measure of the non-thermal motions of the gas). This method assumes small-scale non-thermal motions, thus should not be applied under super-Alfvénic turbulent conditions, i.e., when $\mathcal{M}_A \gg 1$, where \mathcal{M}_A is the Alfvén Mach number. Following Pattle et al. (2020a), it can be expressed as

$$\mathcal{M}_A \approx 3.5 \times 10^{-2} \sigma_\theta, \quad (4)$$

where σ_θ is the polarization angle dispersion in degrees.

When this condition holds, the POS magnetic field strength in μG can thus be estimated using the equation

$$B_{\text{POS}} \approx Q' \sqrt{4\pi\rho} \frac{\sigma_v}{\sigma_\theta} \approx 9.3 \sqrt{n_{\text{H}_2}} \frac{\Delta v_{\text{NT}}}{\sigma_\theta}, \quad (5)$$

where ρ is the mean density of the cloud or subregion in g cm^{-3} ; σ_v is the velocity dispersion in km s^{-1} ; n_{H_2} is the hydrogen molecule number density in cm^{-3} ; and Δv_{NT} is the non-thermal line width in km s^{-1} . In order to simplify the left-hand side of Eq. 5 and arrive at the right-hand side formulation, we followed Crutcher et al. (2004). Under strong B-field conditions ($\sigma_\theta \lesssim 25^\circ$) the factor of $Q' = 0.5$ can provide a somewhat more accurate estimate of the POS field strength (Ostriker et al. 2001; Lai et al. 2002) that Crutcher et al. (2004) also find to be a reasonable value in dense, self-gravitating cores and filaments with expected little field substructure. We again refer the reader to Pattle & Fissel (2019, and references therein) for the discussion on the telescope beam effects that are parameterized in this correction factor, Q' .

We used our Rosette POL-2 data to estimate the polarization angle dispersion. Corresponding molecular line observations of $\text{NH}_3(1,1)$ from the KEYSTONE Survey (Keown et al. 2019, Di Francesco et al., in prep.) were used for deriving the line widths, and we calculated the H_2 volume density from *Herschel*-derived masses.

First, we discuss the dispersion of polarization angles, as this parameter is estimated directly from our POL-2 data. In order to select the magnetic half-vectors, and so the subregion toward which we can derive the field strength, we considered that we need a statistically significant number of half-vectors at $14''$ binning, and we need there to be molecular line observations in the same location. See the coverage of the $\text{NH}_3(1,1)$ data we used in the RMC in Fig. 8, where the ammonia velocity dispersion is over-plotted on the 850 μm Stokes I map.

Taking the above considerations into account led us to only one subregion for which B-field strength estimates were possible. This subregion is indicated by the thick B-field half-vectors in Fig. 9 to the north of REFL08.

We calculated the standard deviation of the polarization angles in the selected group of 25 half-vector seg-

ments. This simple measure for the polarization dispersion is only possible because a priori we chose segments which spread over a relatively narrow range in orientations. The uncertainty of the angle dispersion originates from the median angle uncertainty of the selected individual vectors (see Table 1).

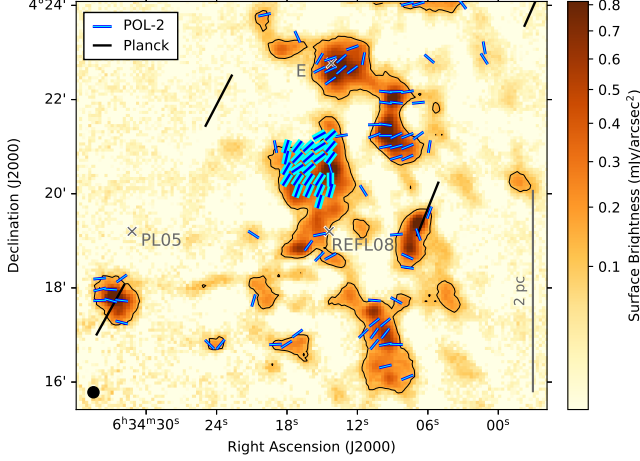


Figure 9. Same as the right-hand panel of Fig. 4 with highlighted B-field half-vectors (in thick sections) in which subregion it was possible to derive the magnetic field strength (see text for details).

The most suitable molecular line data from which we could estimate the line widths were obtained from the KEYSTONE Survey (Keown et al. 2019, Di Francesco et al., in prep.), a large project on the 100-m Green Bank Telescope. This survey is mapping ammonia emission in several giant molecular clouds in order to characterise massive star formation. The spatial resolution of the data cubes is $32''$ projected on $8.8''$ pixel scale, with a spectral resolution of 0.07 km s^{-1} (Keown et al. 2019).

Ammonia molecules are less prone to freezing out than CO at high densities, and their emission lines normally stay optically thin. They can probe deep layers of molecular clouds, and are typically associated with densities above $\sim 10^4 \text{ cm}^{-3}$ (e.g., Benson & Myers 1989).

The FWHM ammonia line width, Δv , was calculated from the velocity dispersion (see Fig. 8) as $\Delta v = \sigma_v \sqrt{8 \ln 2}$. We then separated the non-thermal component Δv_{NT} in km s^{-1} using a similar relation to eqn. B8 of Pattle et al. (2020a).

We estimated an average n_{H_2} volume number density from *Herschel* masses in the subregion which is defined by the selected half-vector segments highlighted in Fig. 9. The *Herschel* mass of this subfield was derived from N_{H_2} column densities as in Sect. 4.1. Then we calculated the volume density following, for example,

Pattle et al. (2020a):

$$n_{\text{H}_2} = \frac{M}{\mu m_{\text{H}}} \frac{3}{4\pi R^3}, \quad (6)$$

where $\mu = 2.8$ is the mean molecular weight per H_2 molecule, m_{H} is the hydrogen atom mass, and R is the radius of a circle with equivalent area of the subfield occupied by the selected vectors.

The derived parameters and their uncertainties relevant to the DCF analysis, along with the estimated Alfvén Mach number and field strength, are summarized in Table 1 for the subregion highlighted by the selected vectors in Fig. 9.

Table 1. Measured and derived properties relevant to the DCF analysis in a subregion of the RMC (see Fig. 9). Abbreviations: *tot* means total, *ave* means average, and *equiv* means equivalent value over the subregion. See text for details.

Property	Value
Pol. angle dispersion, σ_θ	$15.43^\circ \pm 5.33^\circ$
Ammonia line width, Δv_{NT}	$0.97 \pm 0.14 \text{ km s}^{-1}$
H_2 column density, $N_{\text{H}_2}^{\text{tot}}$	$(7.65 \pm 1.53) \times 10^{24} \text{ cm}^{-2}$
H_2 column density, $N_{\text{H}_2}^{\text{ave}}$	$(2.45 \pm 0.49) \times 10^{22} \text{ cm}^{-2}$
Mass of subregion, M^{tot}	$165 \pm 33 M_\odot$
Radius of subregion, R^{equiv}	0.31 pc
H_2 number density, $n_{\text{H}_2}^{\text{ave}}$	$(1.90 \pm 0.38) \times 10^4 \text{ cm}^{-3}$
Alfvén Mach number, \mathcal{M}_{A}	0.54 ± 0.19
B-field strength, B_{POS}	$80 \pm 30 \mu\text{G}$
Mass-to-flux ratio, λ	2.3 ± 1.0

The uncertainties on the column densities, and so on the mass and volume densities, were taken to be 20% in these calculation, in order to avoid the propagation of the typical factor of about 2 systematic errors mainly due to the uncertainties in the dust opacity law. For a more subtle treatment of these systematic errors in the DCF analysis see Pattle et al. (2020a). With other derived properties we use the quadratic addition of errors. Our magnetic field strengths with the DCF method, with assumed resolved structure at the clump level, are found to be typically correct to within a factor of 2, based on numerical simulations by Heitsch et al. (2001). In this factor, only uncertainties originating from the polarization observations (i.e., resolution effects) are considered.

We find the B-field strength toward a dense clump and its outskirts to be $80 \pm 30 \mu\text{G}$ which corresponds to the

range of $50 - 110 \mu\text{G}$. These values are local and thus not clearly representative of the larger environment. The difference in the observed spatial scales and the fact that SCUBA-2 can resolve higher densities are the reasons why we cannot meaningfully compare our results with the *Planck*-found $B_{\text{LOS}} \sim 3 \mu\text{G}$ in the Rosette Nebula (Planck Collaboration XXXIV et al. 2016).

Given that the diffuse ISM shows a well-defined median magnetic field strength of $6.0 \pm 1.8 \mu\text{G}$ (Heiles & Troland 2005), our field is at least an order of magnitude stronger. The B-field strength in this clump and its surroundings seems to be comparable to that of the nearby starless core L1689B (Pattle et al. 2020a), and also to those in the northern and southern parts of the G34 IRDC at a distance of $\sim 3.7 \text{ kpc}$ (Soam et al. 2019). The configuration of our selected subregion for the B_{POS} calculations looks more similar to the geometry of the northern part of the elongated G34 IRDC in that they both contain dense core(s), which are probably already protostellar, as well their surrounding environment. Our magnetic field values are typically comparable to, or weaker than those found in other IRDCs (e.g., Pillai et al. 2015; Liu et al. 2018).

Magnetism is an important component of the ISM, however it is the ratio of mass and magnetic flux that can determine the relative importance of magnetic and gravitational forces, so the stability of the investigated region. We estimated the mass-to-flux ratio, λ , with the formula given by Crutcher et al. (2004):

$$\lambda = 7.6 \times 10^{-21} \frac{N_{\text{H}_2}}{B_{\text{POS}}}, \quad (7)$$

where the average H_2 column density is assumed in cm^{-2} , and B_{POS} in μG .

With the values in Table 1 we derive $\lambda = 2.3 \pm 1.0$, which is higher than the critical value $\lambda = 1$, and suggests that the investigated subregion is gravitationally unstable; the magnetically supercritical B-field is not strong enough to prevent gravitational collapse. This result is not surprising, given that we are in the actively star-forming central ridge of the RMC that is producing high-mass stars.

5. CONCLUSIONS

As part of the BISTRO-2 survey using SCUBA-2/POL-2 at the JCMT, we have presented $850 \mu\text{m}$ polarization observations toward the center of the Rosette Molecular Cloud within an effective area of $\sim 6 \times 7.5 \text{ pc}$ at $\sim 1.6 \text{ kpc}$ distance. Our main results and conclusions are summarized as follows:

1. In our analysis, we used polarization vector selection criteria of Stokes $I > 0$, $I/\delta I > 10$,

$p/\delta p > 3$, and $\delta p < 5\%$, which gave us 152 vectors at $14''$ sampling.

2. We assessed the dust grain alignment through the dependence of polarization fraction on total intensity which shows a $p \propto I^{-\alpha}$ relation. We find $\alpha = 0.49 \pm 0.08$ which suggests that a significant fraction of the dust grains remain aligned with respect to the magnetic field in the highest observed densities.
3. In the north of our region the $850 \mu\text{m}$ image reveals a ring-like structure with a diameter of $\sim 1 \text{ pc}$. Its emission is strongest in the south-west. We refer to this overall structure as a “gemstone ring”, which is seen to be filled with *Spitzer* emission at $3.6 - 24 \mu\text{m}$. This short-to-long wavelength emission forms a gradient that, in places, appears to sit on the SCUBA-2 clumps making up the rim of the bubble wall. The B-field seems to partially trace the circumference of the ring, which turns almost perpendicular to it in the western part where there is a brighter clump.
4. In the southern part of the RMC center, the SCUBA-2 data shows clumpy emission with connecting filaments that follow IRDCs. Here, the POL-2 B-field geometry appears bimodal with some clumps well aligned with the large-scale *Planck* field and some clumps nearly perpendicular.
5. From the $850 \mu\text{m}$ flux densities within our effective mapped area we derive a mass of $\sim 174 M_{\odot}$. We compare our results with large-scale emission-subtracted *Herschel* $250 \mu\text{m}$ -masses and find that the two values agree to within 30%.
6. Using the DCF technique we estimate the POS B-field strength in one subregion of our field, toward a dense clump and its outskirts. We find a value of $80 \pm 30 \mu\text{G}$ that is typically comparable or weaker than the field strength in IRDCs.
7. The mass-to-flux ratio ($\lambda = 2.3 \pm 1.0$) of this sub-field suggests that the B-field is not sufficiently strong to prevent gravitational collapse.

ACKNOWLEDGMENTS

We thank the anonymous reviewer for their helpful suggestions. V.K. and D.W.-T. acknowledge Science and Technology Facilities Council (STFC) support under grant number ST/R000786/1. P.N.D. is funded by the Vietnam National Foundation for Science and Technology Development (NAFOSTED) under grant No. 103.99-2019.368. C.L.H.H. acknowledges the support of the NAOJ Fellowship and JSPS KAKENHI grants 18K13586 and 20K14527. W.K. was supported by the New Faculty Startup Fund from Seoul National University. C.W.L. is supported by the Basic Science Research Program through the NRF funded by the Ministry of Education, Science and Technology (NRF-2019R1A2C1010851). K.Q. is partially supported by National Key R&D Program of China No. 2017YFA0402600, and acknowledges the National Natural Science Foundation of China (NSFC) grant U1731237. The James Clerk Maxwell Telescope is operated by the East Asian Observatory on behalf of the National Astronomical Observatory of Japan; Academia Sinica Institute of Astronomy and Astrophysics; the Korea Astronomy and Space Science Institute (KASI); the Operation, Maintenance and Upgrading Fund for Astronomical Telescopes and Facility Instruments, budgeted from the Ministry of Finance (MOF) of China and administrated by the Chinese Academy of Sciences (CAS); and the National Key R&D Program of China (No. 2017YFA0402700). Additional funding support is provided by the Science and Technology Facilities Council of the United Kingdom and participating universities in the United Kingdom and Canada. SCUBA-2 and POL-2 were built through grants from the Canada Foundation for Innovation. This research used the facilities of the Canadian Astronomy Data Centre operated by the National Research Council of Canada with the support of the Canadian Space Agency. This research has made use of the SIMBAD database, and the “Aladin sky atlas” developed and operated at CDS, Strasbourg Observatory, France. This research has also made use of NASA’s Astrophysics Data System Bibliographic Services.

Facilities: JCMT(SCUBA-2, POL-2), Herschel(SPIRE, PACS), SPITZER(IRAC, MIPS)

Software: APLpy (Robitaille & Bressert 2012), Astropy (Astropy Collaboration et al. 2013), Numpy (Harris et al. 2020), Matplotlib (Hunter 2007), Starlink (Berry et al. 2005; Chapin et al. 2013)

REFERENCES

- Anderson, L. D., Bania, T. M., Balser, D. S., & Rood, R. T. 2011, *ApJS*, 194, 32
- Arthur, S. J., Henney, W. J., Mellema, G., de Colle, F., & Vázquez-Semadeni, E. 2011, *MNRAS*, 414, 1747
- Beckwith, S. V. W., Sargent, A. I., Chini, R. S., & Guesten, R. 1990, *AJ*, 99, 924
- Bell, C. P. M., Naylor, T., Mayne, N. J., Jeffries, R. D., & Littlefair, S. P. 2013, *MNRAS*, 434, 806
- Benson, P. J., & Myers, P. C. 1989, *ApJS*, 71, 89

- Berry, D. S., Gledhill, T. M., Greaves, J. S., & Jenness, T. 2005, in *Astronomical Society of the Pacific Conference Series*, Vol. 343, *Astronomical Polarimetry: Current Status and Future Directions*, ed. A. Adamson, C. Aspin, C. Davis, & T. Fujiyoshi, 71
- Bica, E., Dutra, C. M., & Barbuy, B. 2003, *A&A*, 397, 177
- Broos, P. S., Getman, K. V., Povich, M. S., et al. 2013, *ApJS*, 209, 32
- Cambr  sy, L., Marton, G., Feher, O., T  th, L. V., & Schneider, N. 2013, *A&A*, 557, A29
- Chandrasekhar, S., & Fermi, E. 1953, *ApJ*, 118, 113
- Chapin, E. L., Berry, D. S., Gibb, A. G., et al. 2013, *MNRAS*, 430, 2545
- Chen, Z., Jiang, Z., Tamura, M., Kwon, J., & Roman-Lopes, A. 2017, *ApJ*, 838, 80
- Costa, A. H., Spangler, S. R., Sink, J. R., Brown, S., & Mao, S. A. 2016, *ApJ*, 821, 92
- Coud  , S., Bastien, P., Houde, M., et al. 2019, *ApJ*, 877, 88
- Crutcher, R. M., Nutter, D. J., Ward-Thompson, D., & Kirk, J. M. 2004, *ApJ*, 600, 279
- Currie, M. J., Berry, D. S., Jenness, T., et al. 2014, in *Astronomical Society of the Pacific Conference Series*, Vol. 485, *Astronomical Data Analysis Software and Systems XXIII*, ed. N. Manset & P. Forshay, 391
- Cutri, R. M., & et al. 2012, *VizieR Online Data Catalog*, II/311
- Cutri, R. M., Skrutskie, M. F., van Dyk, S., et al. 2003, *VizieR Online Data Catalog*, II/246
- Davis, L. 1951, *Physical Review*, 81, 890
- Dent, W. R. F., Hovey, G. J., Dewdney, P. E., et al. 2009, *MNRAS*, 395, 1805
- Di Francesco, J., Johnstone, D., Kirk, H., MacKenzie, T., & Ledwosinska, E. 2008, *ApJS*, 175, 277
- di Francesco, J., Sadavoy, S., Motte, F., et al. 2010, *A&A*, 518, L91
- Friberg, P., Bastien, P., Berry, D., et al. 2016, in *Society of Photo-Optical Instrumentation Engineers (SPIE) Conference Series*, Vol. 9914, *Millimeter, Submillimeter, and Far-Infrared Detectors and Instrumentation for Astronomy VIII*, 991403
- Friberg, P., Berry, D., Savini, G., et al. 2018, in *Society of Photo-Optical Instrumentation Engineers (SPIE) Conference Series*, Vol. 10708, *Millimeter, Submillimeter, and Far-Infrared Detectors and Instrumentation for Astronomy IX*, ed. J. Zmuidzinas & J.-R. Gao, 107083M
- Guillet, V., Girart, J. M., Maury, A. J., & Alves, F. O. 2020, *A&A*, 634, L15
- Harris, C. R., Millman, K. J., van der Walt, S. J., et al. 2020, *Nature*, 585, 357
- Heiles, C., & Troland, T. H. 2005, *ApJ*, 624, 773
- Heitsch, F., Zweibel, E. G., Mac Low, M.-M., Li, P., & Norman, M. L. 2001, *ApJ*, 561, 800
- Hennemann, M., Motte, F., Bontemps, S., et al. 2010, *A&A*, 518, L84
- Hensberge, H., Pavlovski, K., & Verschueren, W. 2000, *A&A*, 358, 553
- Hildebrand, R. H. 1983, *QJRAS*, 24, 267
- Hoang, T., & Lazarian, A. 2016, *ApJ*, 831, 159
- Holland, W. S., Bintley, D., Chapin, E. L., et al. 2013, *MNRAS*, 430, 2513
- Houde, M., Hull, C. L. H., Plambeck, R. L., Vaillancourt, J. E., & Hildebrand, R. H. 2016, *ApJ*, 820, 38
- Hull, C. L. H., & Zhang, Q. 2019, *Frontiers in Astronomy and Space Sciences*, 6, 3
- Hunter, J. D. 2007, *Computing in Science and Engineering*, 9, 90
- Jenness, T., Chapin, E. L., Berry, D. S., et al. 2013, *SMURF: Submillimeter User Reduction Facility*, , , ascl:1310.007
- Jones, T. J., Bagley, M., Krejny, M., Andersson, B. G., & Bastien, P. 2015, *AJ*, 149, 31
- Keown, J., Di Francesco, J., Rosolowsky, E., et al. 2019, *ApJ*, 884, 4
- Kharchenko, N. V., Piskunov, A. E., Schilbach, E., R  ser, S., & Scholz, R. D. 2013, *A&A*, 558, A53
- Kirchschlager, F., Bertrang, G. H. M., & Flock, M. 2019, *MNRAS*, 488, 1211
- Kirk, J. M., Ward-Thompson, D., & Crutcher, R. M. 2006, *MNRAS*, 369, 1445
- K  nyves, V., Andr  , P., Men'shchikov, A., et al. 2015, *A&A*, 584, A91
- K  nyves, V., Andr  , P., Arzoumanian, D., et al. 2020, *A&A*, 635, A34
- Lai, S.-P., Crutcher, R. M., Girart, J. M., & Rao, R. 2002, *ApJ*, 566, 925
- Lasker, B. M., Sturch, C. R., McLean, B. J., et al. 1990, *AJ*, 99, 2019
- Lazarian, A., & Hoang, T. 2007, *MNRAS*, 378, 910
- Liu, T., Kim, K.-T., Liu, S.-Y., et al. 2018, *ApJL*, 869, L5
- Lombardi, M., Alves, J., & Lada, C. J. 2011, *A&A*, 535, A16
- Mairs, S., Johnstone, D., Kirk, H., et al. 2015, *MNRAS*, 454, 2557
- Martins, F., Mahy, L., Hillier, D. J., & Rauw, G. 2012, *A&A*, 538, A39
- Matthews, B. C., McPhee, C. A., Fissel, L. M., & Curran, R. L. 2009, *ApJS*, 182, 143
- Motte, F., Zavagno, A., Bontemps, S., et al. 2010, *A&A*, 518, L77

- Mužić, K., Scholz, A., Peña Ramírez, K., et al. 2019, *ApJ*, 881, 79
- Ogura, K., & Ishida, K. 1981, *PASJ*, 33, 149
- Ostriker, E. C., Stone, J. M., & Gammie, C. F. 2001, *ApJ*, 546, 980
- Park, B.-G., & Sung, H. 2002, *AJ*, 123, 892
- Pattle, K., & Fissel, L. 2019, *Frontiers in Astronomy and Space Sciences*, 6, 15
- Pattle, K., Ward-Thompson, D., Kirk, J. M., et al. 2015, *MNRAS*, 450, 1094
- Pattle, K., Ward-Thompson, D., Berry, D., et al. 2017, *ApJ*, 846, 122
- Pattle, K., Lai, S.-P., Hasegawa, T., et al. 2019, *ApJ*, 880, 27
- Pattle, K., Lai, S.-P., Di Francesco, J., et al. 2020a, *arXiv e-prints*, arXiv:2011.09765
- Pattle, K., Lai, S.-P., Wright, M., et al. 2020b, *arXiv e-prints*, arXiv:2009.14758
- Pérez, M. R. 1991, *RMxAA*, 22, 99
- Perez, M. R., The, P. S., & Westerlund, B. E. 1987, *PASP*, 99, 1050
- Phelps, R. L., & Lada, E. A. 1997, *ApJ*, 477, 176
- Pillai, T., Kauffmann, J., Tan, J. C., et al. 2015, *ApJ*, 799, 74
- Planck Collaboration XXXIV, Aghanim, N., Alves, M. I. R., et al. 2016, *A&A*, 586, A137
- Planck Collaboration XXXV, Ade, P. A. R., Aghanim, N., et al. 2016, *A&A*, 586, A138
- Poulton, C. J., Robitaille, T. P., Greaves, J. S., et al. 2008, *MNRAS*, 384, 1249
- Povich, M. S., Stone, J. M., Churchwell, E., et al. 2007, *ApJ*, 660, 346
- Robitaille, T., & Bressert, E. 2012, *APLpy: Astronomical Plotting Library in Python*, , ascl:1208.017
- Román-Zúñiga, C. G., Elston, R., Ferreira, B., & Lada, E. A. 2008, *ApJ*, 672, 861
- Román-Zúñiga, C. G., & Lada, E. A. 2008, *Star Formation in the Rosette Complex*, ed. B. Reipurth, Vol. 4, 928
- Roy, A., André, P., Palmeirim, P., et al. 2014, *A&A*, 562, A138
- Savage, A. H., Spangler, S. R., & Fischer, P. D. 2013, *ApJ*, 765, 42
- Schneider, N., Motte, F., Bontemps, S., et al. 2010, *A&A*, 518, L83
- Schneider, N., Csengeri, T., Hennemann, M., et al. 2012, *A&A*, 540, L11
- Simpson, R. J., Povich, M. S., Kendrew, S., et al. 2012, *MNRAS*, 424, 2442
- Soam, A., Liu, T., Andersson, B. G., et al. 2019, *ApJ*, 883, 95
- Townsley, L. K., Feigelson, E. D., Montmerle, T., et al. 2003, *ApJ*, 593, 874
- Tremblin, P., Minier, V., Schneider, N., et al. 2013, *A&A*, 560, A19
- Tremblin, P., Schneider, N., Minier, V., et al. 2014, *A&A*, 564, A106
- Wang, J., Feigelson, E. D., Townsley, L. K., et al. 2009, *ApJ*, 696, 47
- Ward-Thompson, D., Pattle, K., Bastien, P., et al. 2017, *ApJ*, 842, 66
- Whittet, D. C. B., Hough, J. H., Lazarian, A., & Hoang, T. 2008, *ApJ*, 674, 304
- Williams, J. P., Blitz, L., & Stark, A. A. 1995, *ApJ*, 451, 252
- Ybarra, J. E., Lada, E. A., Román-Zúñiga, C. G., et al. 2013, *ApJ*, 769, 140
- Ybarra, J. E., & Phelps, R. L. 2004, *AJ*, 127, 3444